A computational approach to simulate the optical and thermal performance of a novel complex geometry solar tower molten salt cavity receiver

M. Slootweg, K.J. Craig* and J.P. Meyer
Clean Energy Research Group
University of Pretoria, Pretoria, South Africa +27-12-420-3515
* Corresponding author: ken.craig@up.ac.za

Abstract

A novel complex geometry solar tower molten salt cavity receiver is presented and investigated with regard to its optical and thermal performance. The receiver's design consists of a collector with the goal of limiting the concentrated rays from escaping, which is further enhanced by an absorber design that consists of an array of hexagonal pyramid elements inspired by Garbrecht, et al. (2013) that limits re-radiative and convective losses. The performance analysis considers the solar position, DNI and sun shape with an existing heliostat field (PS-10 field) to analyse the receiver, rather than assuming a flux. The optical analysis is conducted with the Monte Carlo ray-tracing approach, while the thermal analysis is conducted using computational fluid dynamics (CFD). The initial design showed impractical receiver efficiencies of 32.8%, while preliminary sensitivity studies on selected parameters increased efficiencies up to 69.9%. In the process a design with improved optics was developed and proposed, with initial results increasing efficiencies up to 82.4%. The study indicates that the design is promising from a heat transfer point of view, although many improvements are still to be made to the design to make it competitive.

Keywords: Concentrated solar power; Central receiver, CFD; Monte Carlo ray-tracing; Molten salt

1   Introduction

The increased concerns over the altering climate due to the release of anthropogenic greenhouse gases have caused a major shift in the developments of renewable technologies, which include solar technologies such as concentrating solar power (CSP) plants. Central receiver CSP systems, also commonly referred to as solar tower CSP systems, have been receiving increased attention by researchers, with this technology being predicted to indicate the greatest margin for technological improvement (40-65% is estimated), with the improvement of the receiver technology potentially providing the greatest contribution to better efficiencies (EASAC, 2011).

Solar tower power plants consist of a centralized elevated structure with a receiver (usually) mounted on top of it, surrounded by an array of dual-axis tracking mirrors called heliostats, which are spaced in such a way to avoid mechanical or optical interference, with the goal to reflect the incident solar radiation to the elevated receiver or secondary optical reflector. The concentrated radiation incident on the absorber is then absorbed and transferred to the heat transfer fluid (HTF). Losses at the absorber area occur due to a fraction of the incident radiation that get reflected. Thermal losses also occur due to the heated surface of the absorber causing thermal emission or re-radiation, as well as convection and, to a limited extent, conduction. Convection losses can be divided into natural convection (buoyancy-induced) and forced convection (wind). Conduction is limited to heat leaking into the tower structure. If the receiver is equipped with a secondary concentrator, such as a compound parabolic concentrator (CPC), the absorption of the concentrator's reflective surface also contributes to the receiver's losses. The losses are summarised in equation (1):

$$\dot{Q}_{loss,receiver} = \left(\dot{Q}_{refl.} + \dot{Q}_{conv.} + \dot{Q}_{rad.} + \dot{Q}_{cond.} \right)_{absorber} + \dot{Q}_{abs.,concentrator} \quad (1)$$

The heat that does not get lost is absorbed by the HTF and transferred to the point of application. With the development of receiver technology, a great variety of designs have been proposed, all with their own type of HTF, which include air, water/steam, molten salts, and liquid sodium (although sodium was never implemented commercially due to its high combustibility when in contact with water) (Lovegrove & Stein, 2012; Ho & Iverson, 2014). For the liquid HTF, only two types of receiver designs have been realized: external and cavity receivers, while the gas HTF receivers have adopted more complex designs to overcome the poor heat transfer properties that gas HTFs such as air hold.

External or open tubular receivers are panels of parallel-aligned tubes (usually) arranged like a cylinder on top of the tower. The concentrated radiation incident on the outer surface of these panels is then absorbed by the HTF circulating through the tubes. This simplistic design makes it easy to manufacture and assemble, and provides the freedom to easily adjust the design to accommodate a wide variety of liquid HTFs. External receivers have been developed to be as visible as possible for the heliostats to allow for the receiver to be exposed to the reflected radiation to the maximum from all angles. This exposure, however, allows for an increase in thermal emissions due to the large view factor, as well as an increase in convection losses due to receiver area being exposed to air flow passing unopposed across the surface of the receiver. These losses become especially more apparent as the technology develops to allow for higher HTF outlet temperatures, which would be a result of higher surface temperatures, to increase the Rankine cycle efficiency, following Carnot's theorem (Ho & Iverson, 2014). The earliest implementation of external receivers were with the International Energy Association/Small Solar Power Systems (IEA/SSPS) in Spain (1981) and the Solar One power plant in Barstow, CA, USA (1982), with the former having used liquid sodium (and facilitated cavity receivers too) and the latter steam as HTF (Kesselring & Selvage, 1986; Pacheco, et al., 2002). The first implementation of molten salt as HTF was with the Solar Two demonstration project (1996); a project that was upgraded from the Solar One project (Pacheco, et al., 2002). Since then, commercial installations of external receivers have been implemented. Much research has been conducted to improve the external receiver design, which include: optimal dimensions and parameters (Lata, Rodriquez, & de Lara, 2008; Rodríguez-Sánchez M. , Sánchez-González, Marugán-Cruz, & Santana, 2014; Rodríguez-Sánchez M. , Sánchez-González, Acosta-Iborra, & Santana, 2017), analysis and minimization of thermal losses (Rodríguez-Sánchez, Soria-Verdugo, Almendros-Ibáñez, Acosta-Iborra, & Santana, 2014; Rodríguez-Sanchez, Marugan-Cruz, Acosta-Iborra, & Santana, 2014; Pye, Zheng, Asselineau, & Coventry, 2014), coating materials (Joly, et al., 2013) and the selection of HTF (Pacio & Wetzel, 2013; Forsberg, Peterson, & Zhao, 2007; Singer, Buck, Pitz-Paal, & Müller-Steinhagen, 2010).

Cavity receivers provide an alternative in design to external receivers to limit the losses evident at external receivers. These receiver's absorber, which with current applications only have tubular panels like the external receiver, is situated within an enclosure, allowing the concentrated rays to enter through a single opening called an aperture. This design shields the absorber surface from the elements, therefore limiting convection losses. The configuration of the absorber inside the cavity also allows the receiver to capture most of the reflected and emitted radiation. The drawback, however, is that the receiver has a limited acceptance angle for concentrated rays and is therefore limited to polar fields. To apply a cavity receiver to a heliostat field with a wider acceptance angle would therefore require the installation of more than one receiver. The first commercial implementation of a cavity receiver was with the PS-10 power plant in Seville, Spain (2007), using steam as HTF (European Union, 2007), and is commonly chosen as the standard case plant for central receiver research. Research conducted on cavity receivers include the effects of natural convection (Clausing, 1981), forced convection (Fang, Wei, Dong, & Wang, 2011) and radiation (Yu, Wang, & Xu, 2012) on the receiver, and how these factors could be limited (Chang, Li, Xu, Chang, & Wang, 2014; Li, Kong, Wang, Chang, & Bai, 2010). Also, research on heat transfer enhancement in receivers is a much-researched topic (Montes, Rovira, Martínez-Val, & Ramos, 2012; Liao & Faghri, 2016).

Receivers that use gases as HTF require completely other designs to overcome the low thermal conductivity and the high temperatures associated with them. A gas receiver that has been researched and developed since the 1990s is the volumetric receiver: a receiver that is filled with porous shapes, foam, knit-wire packs or foil arrangements. The concentrated radiation is absorbed by the volumetric porous substance, by heating the material in the volume. The gas HTF then heats up as it passes through the volume (Avila-Marin, 2011). A more recent development in gas receivers is the tubular gas receiver: a cavity receiver with absorber tubes designed and arranged to allow for the concentrated radiation to heat the gas inside the tubes the most effectively, without the high temperatures resulting in thermal losses. Tubular gas receiver prototypes developed by the DLR include the SOLHYCO-receiver (Amsbeck, Buck, Heller, Jedamski, & Uhlig, 2008) and the Solugas receiver (Korzynietz, Quero, & Uhlig, 2012).

To overcome the challenges of thermal losses, many different designs have been proposed. The SCRAP receiver is an air receiver design proposed by the STERG group of the University of Stellenbosch. The receiver can be described as a collection of tubular absorber assemblies, or spikes, concentrically distributed to form a "porcupine"-effect, where the spike density increases as one approaches the centre of the receiver. The cold air impinges at the tip of the spike from an inner tube within the spike, after which it flows back into the outer tube as it gets heated by the incident radiation on the outer shell of the spike (Lubkoll, Backström, Harms, & Kröger,

2015). A similar concept is a design proposed by Garbrecht, et al. (2013), where an array of hexagonal pyramid-shaped elements are arranged in a honeycomb structure, their apexes pointing outwards in the direction of the heliostat field. As with the SCRAP receiver, the cold fluid (molten salt) is impinged into the tip of the pyramid by an inner tube, after which it flows next to the inner surface of the pyramid, absorbing the concentrated radiation incident on the pyramid outer surface (Garbrecht, Al-Sibai, Kneer, & Wieghardt, 2013). These two designs provide the advantages of limiting re-radiation losses due to a lower view factor and other factors, as well as limited convection due to the designs' elements bifurcating the air flow. Other proposed designs include the REFOS closed-loop volumetric receiver (Buck, et al., 2002), RPC pressurised air receiver (Hischier, Hess, Lipinski, Modest, & Steinfeld, 2009), hybrid pressurised air receiver (Kretzschmar & Gauché, 2012) and falling film receivers (Ho & Iverson, 2014), just to name a few.

The present work focuses on a novel solar tower molten salt cavity receiver design-idea. The testing and development of this design takes a realistic approach, taking into consideration the solar position and DNI for different times of the year based on the position of a representative heliostat field (PS-10, Seville, Spain), and then coupling the optical results incident on the receiver to the thermal analysis, which is a more comprehensive design process than assuming a standard incident flux that is usually done with the development of receivers.

2 New receiver design

The new proposed solar tower molten salt cavity receiver concept's main goal is to minimize the thermal losses that occur in solar tower receivers, which are predominantly re-radiative and convective losses. Therefore, a cavity design has been proposed with the goal of limiting the incident rays that enter the aperture from escaping, while also limiting the re-radiative and convective losses at the absorber area. The absorber design is inspired by work done by Garbrecht, et al. (2013) and Lubkoll, et al. (2015), using jet impingement heat transfer at the the absorber, while the REFOS receiver design by Buck, et al. (2002) inspired the receiver's optics.

(a)   (b)
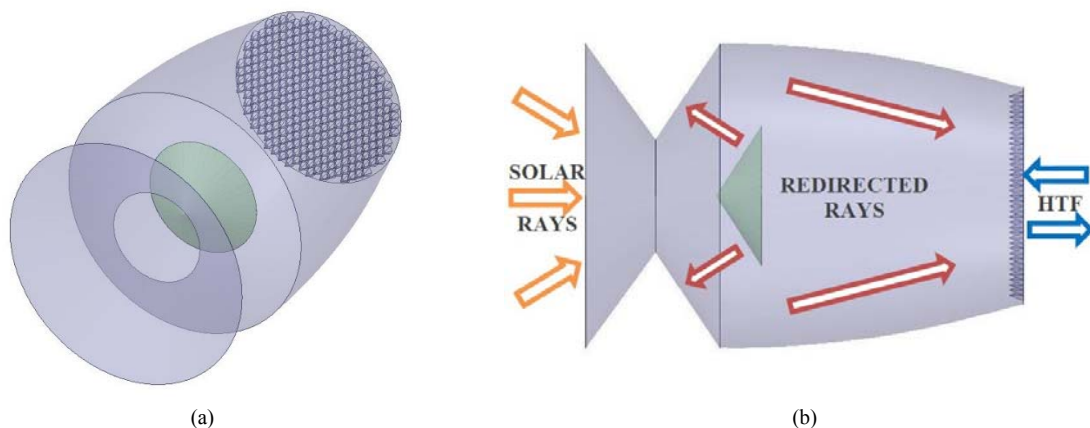
Fig. 1. The novel solar tower molten salt cavity receiver concept proposed with (a) displaying the proposed model in 3D; and (b) a side view with the basic workings illustrated.

The proposed receiver design is illustrated in Fig. 1, with Fig. 1a displaying the design in 3-D. As is illustrated in Fig. 1b, the rays that enter the aperture of the receiver get reflected to the cavity area of the receiver. The rays get deflected by the reflective surfaces to the point where they reach the absorber area of the receiver. The reflective surface is also insulated with ceramic fibre material, a common insulating material used for high temperature applications. Currently, secondary collector reflective surfaces for point-focus applications are mostly dependent on cooling mechanisms to reduce stress and degradation due to high thermal gradients (Fernández-García, et al., 2014). There is, however, ongoing research to improve these materials. Since this is not the focus of this study, certain assumptions was made regarding the properties of the reflective surface during this research. The absorber consists of a multitude of hexagonal pyramid-shaped elements that are arranged in a honeycomb structure, their apexes pointing in the direction of the aperture. It is within these pyramid elements that the incident radiation on the surface of the absorber is transferred to the HTF. The purpose of the cavity of the receiver is predominantly to limit the effects of convection losses on the performance of the receiver, but also to stop the reflection and re-radiation of energy, while the multiple hexagonal pyramid-shaped matrix absorber design is there to minimize the re-radiation effects, since the pyramid areas capture the neighbouring radiative

losses, and to maximize the heat transfer by making use of jet impingement, which provides superior heat transfer capabilities.

The structure of the pyramid element is displayed in Fig. 2, and is similar to the design proposed by Garbrecht, et al. (2013). With the cool HTF entering through the central pipe situated inside the pyramid (blue arrow), it gets injected at the tip of the pyramid. By having the coolest HTF at the tip ensures less losses at the tip, which is beneficial, since the tip of the pyramids structure's heat losses are the losses least likely to be captured by neighbouring pyramids. Also take note that a concave surface was added in the tip of the pyramid, while a similar design by Garbrecht et al. (2013) did not include this. This was done to prevent the fluid stagnating in the tip to heat up to unwanted levels, as well as to make use of the advanced heat transfer mechanism of jet impingement heat transfer. The central pipe was also given a smaller diameter in the test case compared to the design of Gabrecht et al. (2013), to further enhance the heat transfer at the tip, since Garbrecht reported that the tip showed unwanted temperatures and poor heat transfer. After impinging at the tip of the element, the HTF flows in a gap next to the thin shell that seperates the fluid from the surroundings to absorb the incident radiation on the absorber's surface. The detail of the design will be further elaborated on in subsequent sections.
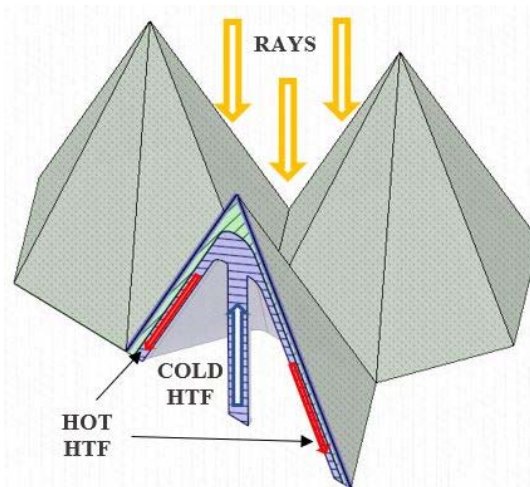

Fig. 2. Close-up view of an exemplary arrangement of the absorber structure, with the one element shown with a sectioned view. The blue zone illustrates the HTF region and the green the absorber shell.

It should be noted that this receiver is a conceptual design, with the main purpose of presenting an alternative approach to combat some of the challenges that current solar tower receiver designs face from an energy transfer point of view. The feasibility of certain technical aspects which include the structural design, heat transfer fluid consideration and drainage and how the flow connects to the rest of the plant, as well as the techno-economic feasibility, have not been included in this study and should be considered in future studies.

3   Modelling and numerical setup
As was mentioned in the *Introduction*, to conduct a numerical performance analysis of a receiver, one would need to implement models to replicate the subject of matter to a satisfactory accuracy. Therefore, the factors that need to be considered for a performance analysis throughout the year are the solar field (for a realistic flux distribution), the sun's position and direct normal irradiance (DNI) throughout the year, as well as its sun shape. The assumption of a pillbox sun shape was given with an angle of 4.65 mrad. As the main tool of the optical modelling and investigation, the free Monte Carlo ray-tracing software environment SolTrace was used (Wendelin, Dobos, & Lewandowski, 2013). Furthermore, the thermal analysis follows the optical analysis at the absorber of the receiver. These simulations were conducted using the commercial Computational Fluid Dynamics (CFD) code Fluent 19.1 by ANSYS, Inc.

3.1   *Heliostat field test case model*
A solar power plant that has undergone an extensive amount of research on several aspects of central receiver design development is the Planta Solar 11 MW central receiver solar power plant (PS-10) situated near Seville, Spain. It is with this reason, as well as it being a polar field (since the receiver is a cavity design), that the PS-10 heliostat field was chosen as the reference test case field. Take note that the purpose of the field is to provide a realistic flux distribution for the receiver. For the field to be simulated in SolTrace, as well as to implement solar

tracking and DNI models, the parameters and dimensions that are summarised in Table 1 are needed. Although the parameters displayed in Table 1 do not indicate the exact figures of some dimensions and properties, they do give a close resemblance of the values that the field might have. This is verified with sources such as Eddhibi, et al. (2015), Noone, et al. (2012) and Osuna, et al. (2006). The coordinates of the heliostats relative to the tower was also obtained from Noone, et al. (2012). For the focal length, the assumption was made that all heliostats were identical. For the PS-10 field, the average distance between the heliostats and the aperture was 400.9 m, with a median of 377.9 m. The assumption was therefore made to apply an approximate average of both values for a focal length of 390 m to all heliostats. Take note that the given aperture angle changes in the study to value of 24°, after the study concluded that this showed to be the optimal angle for the given field.

Table 1
Input parameters for the modelling of the PS-10 solar power plant heliostat field.

Location	Latitude [°]	37.44 [North]
	Longitude [°]	6.25 [West]
	Altitude [m]	7
	Greenwich Mean Time (GMT) [hours]	+1/+2*
Tower	Height [m]	115
Aperture	Angle [°]	11.5/12.5**
	Width [m]	13.78
	Height [m]	12
Heliostat	Type	Sanlúcar 120
	Width [m]	12.84
	Height [m]	9.45
	Reflectivity	0.88
	Transmissivity	0
	Slope error	0.71
	Specularity error	0.14
	Error type	Gaussian

* Central European Time (CET), the time being used by Spain, observes Daylight Saving Time (DST), which causes this fluctuation in GMT
** Value changes during study

3.2 Solar position model

The sun's position changes its interaction with the heliostat field, and therefore provides a different flux at different times. The DNI is also a function of the sun's position. The accurate modelling of the sun's position relative to the heliostat field is therefore of great importance. The model implemented for this is the one developed by Spencer (1971) and proposed by Iqbal (1983) as was adequate for the purpose of investigation (Reda & Andreas, 2004). The model assumes the Earth rotates around the Sun in an elliptical orbit, and that this orbit remains constant for a long period of time, therefore omitting factors such as celestial bodies, leap years etc.

The sun's position in solar tracking is commonly given with two variables: the zenith (θ) and azimuth (ψ) angle. The zenith angle is the angle between the local zenith (the observer's position on the Earth's surface) and the line joining the observer's point and the sun. The azimuth angle is measured at the local zenith between the plane formed by the line between the observer and the sun and the line between the observer and the local zenith, as well as the plane formed by the circle passing through the observer's poles and the zenith (observer's meridian). Refer to literature such as *An introduction to solar radiation* by Iqbal (1983) for a more detailed description with illustrations. The equations formulated for the implemented solar position model are also given by Iqbal (1983).
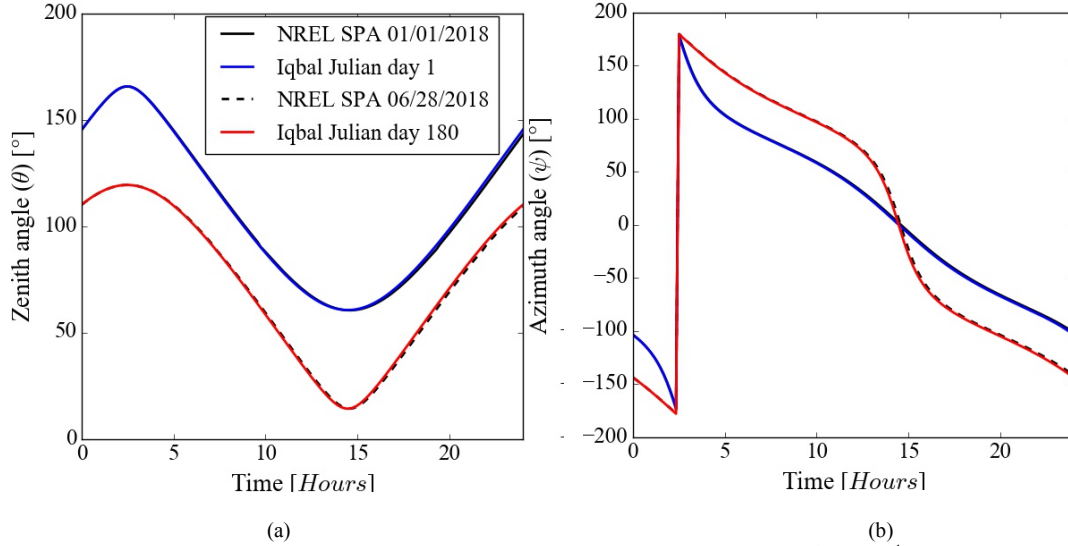
Fig. 3. A graphical representation of the (a) Zenith angles (θ) and (b) Azimuth (ψ) angles for the 1st and 180th Julian day, comparing the Iqbal model to the NREL's MIDC Solar Position Algorithm (SPA) (NREL, 2018)

When comparing the Iqbal model to the National Renewable Energy Laboratory's (NREL) Measurements & Instrumentation Data Centre (MIDC) Solar Position Algorithm (NREL, 2018), which is based on work done by Reda & Andreas (2004), it is clear that the model correlates well, with errors negligible for application purposes.

3.3   Direct Normal Irradiance model

Modelling the DNI of any location provides challenges that are almost unsolvable due to the significant role that the weather plays in the solar irradiation. To overcome this challenge, the assumption can be made for a cloudless-sky atmosphere model. This assumption makes sense for the intended study, since CSP plants are only functional during times when there is a level of radiation above a certain threshold level. A review done by Iqbal (1983) included a summary of the clear-sky direct-insolation models presented by Bird & Hulstrom (1981), which concluded that the Parameterisation Model C produced the most accurate results, and was hence chosen as the model that would be used to determine the DNI. For this model, the irradiance is a function of the eccentricity correction factor as well as the transmittance of different variables. The variables include the transmittance to direct irradiance due to:

- Rayleigh scattering effects of air molecules (τ_r)
- Absorption by ozone (τ_o)
- Absorption by uniformly mixed gases (τ_g)
- Absorption by water vapour (τ_w)
- Attenuation by aerosols (τ_a)

The DNI, expressed as I_n, can be calculated with equation (2):

$$I_n = 0.9751E_0 I_{sc}\tau_r\tau_o\tau_g\tau_w\tau_a \qquad (2)$$

The solar constant (I_{sc}), which is the rate of total solar energy at all wavelengths incident on a unit area exposed normally to the sunrays, is recommended as 1367 W/m^2 by Fröhlich and colleagues (Frohlich & Brusa, 1981; Frohlich & Wehrli, 1981). As with the solar position model, the details regarding the equations and the implementation of the Parameterisation Model C clear sky DNI model are given by Iqbal (1983). With the calculation of τ_w, a constant year-averaged temperature and humidity is assumed. The authors, however, wanted to model this more accurately. By obtaining the monthly average minimum and maximum temperature as well as the humidity of the location, a fourth-order discrete trigonometric approximation was applied. This resulted in the graph displayed in Fig. 4. The daily temperature fluctuation was approximated by the WAVE method initially presented by De Wit, et al. (1978), which was the most accurate method according to a study done by Reicosky, et al. (1989).
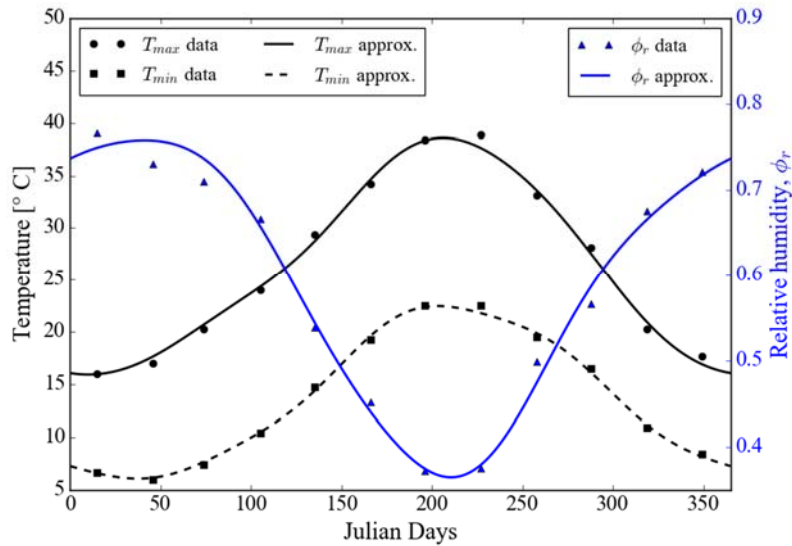
Fig. 4. Fourth-order discrete trigonometric approximation of the averaged maximum and minimum temperature as well as the relative humidity annual fluctuations of Seville, Spain.

The clear sky DNI parametrization C model was compared to SOLERGY generated data (an interpolated derivative of weather data) for two different times of the year (2nd of January and 6th of June) (Romero, Marcos, Osuna, & Fernandez, 2000). This is shown Fig. 5. The model is limited to a zenith angle of 85°, and therefore any value calculated with a zenith angle greater than 85° is deemed unfit (represented with the grey lines in Fig. 5). Referring to the graph in Fig. 5, the model follows the trend of the weather data, although not accurately predicting the DNI for all times of the day. This is to be expected, since the model is based on the clear sky assumption, meaning that clouds or other weather interferences are not included in the model. It is also with this reason that the SOLERGY data, especially the data representing the 2nd of January, display a non-smooth fluctuation throughout the day. There is also a noticeable jump in the modelled DNI at the local apparent time of 14:00. This is due to the WAVE method implemented that models the hourly temperature fluctuations of a given day and location. This method has a non-continuous step at 14:00, which again reflects in the DNI. The purpose of the DNI model in the research conducted is not to accurately predict the DNI throughout the year, but rather to give realistic DNI fluctuations that can be used to test CSP technologies accurately in a numerical environment. The model has shown to provide just that.
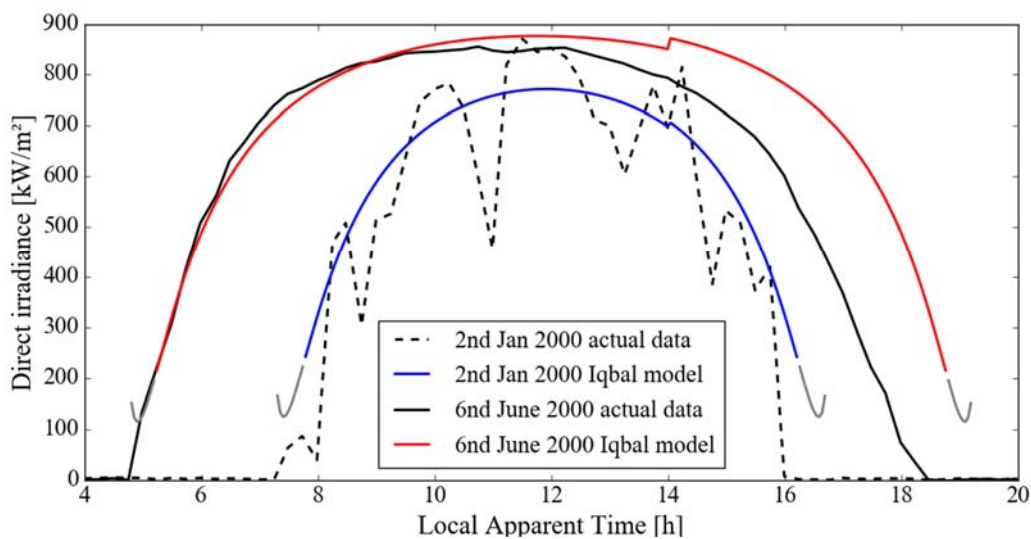

Fig. 5. The Iqbal clear-sky direct-insolation Parameterisation model C is graphically displayed for a day-period, with a winter's and summer's day compared to SOLERGY generated data (Romero, Marcos, Osuna, & Fernandez, 2000). The zenith angle limit was set at 85°.

3.4 Receiver optical setup

The receiver's complex structure is designed to 'trap' the concentrated solar rays. SolTrace, however, only provides standard or primitive geometries to approximate models. To model this receiver, and other complex geometries in general, within SolTrace is therefore limited to geometry approximations. To overcome this, a new approach is developed to discretize the intended geometry into smaller parts. Inspired by work done by Craig, et al. (2016), the discretization is done by meshing the intended geometry using tetrahedrons in the ANSYS meshing environment. Then, instead of constructing circular disks in the SolTrace environment with every disc's centre positioned at the centroid of each mesh (Craig, Marsberg, & Meyer, 2016), the surface mesh file is converted to irregular triangles positioned and constructed in the same location as its original mesh element, but within SolTrace using the scripting environment. Therefore, to obtain a more accurate approximation of the surface of the geometry, the mesh can be refined. This approach also provides the added benefit of converting the optical results to a flux approximation for a thermal analysis by averaging each element's flux and assigning that local flux to the element's centroid, which can be converted to an interpolation file that can be applied to thermal analysis. An example of the approach to 'discretize' an absorber surface is shown in Fig. 6.
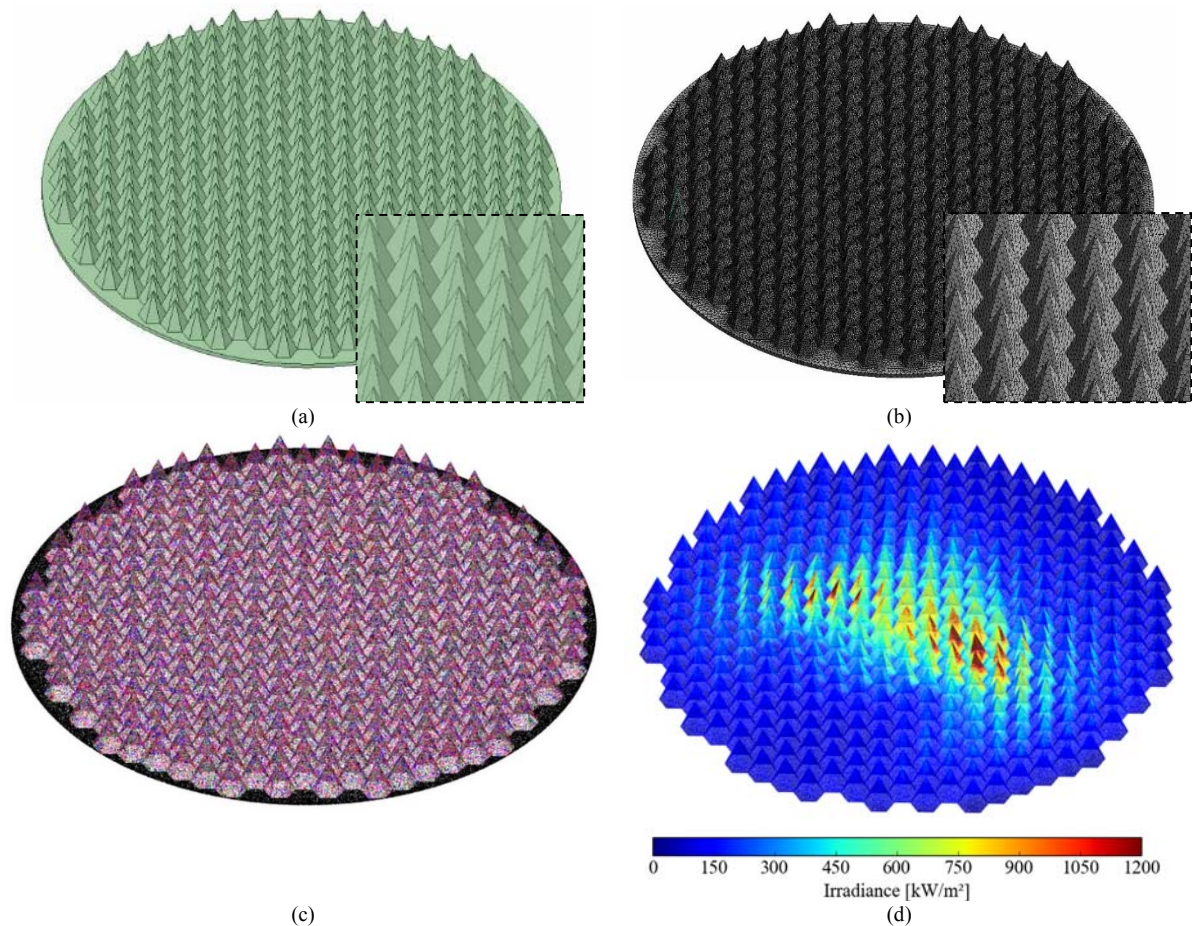

Fig. 6. Illustration of the conversion of (a) a complex geometry using (b) a tetrahedral mesh to simulate the model within (c) SolTrace using irregular triangles to finally obtain (d) a flux distribution that could be applied to a thermal analysis (the image is an isometric view of the flux shown in Fig. 14).

In SolTrace, an increase in elements simulated increases the time of simulations. Therefore, to simulate the receiver, all surfaces that could be accurately approximated by primitive shapes were identified to reduce the number of elements. This resulted in all surfaces, with the exception of the absorber area consisting of an array of hexagonal pyramids, to be modelled using single primitive bodies. Even the collector's curved shape was accurately approximated by a parabolic curve. From initial analyses using ray tracing it was also clear that the collector cone in front of the aperture did not provide any significant improvement to the design, and was therefore excluded during the analysis. The results of these initial analyses have not been included in this paper. Generally, to approximate a surface by discretizing it into smaller elements would require a mesh study to determine what mesh size is satisfactory for the given surface. Since only the absorber area needs to be approximated, which consists of only flat surfaces, no mesh study needs to be conducted for the surface's approximation, since the

elements that approximate the surface are themselves flat. The mesh should, however, be considered when approximating the flux on the absorber for the thermal analysis.

The optical properties assigned to the receiver are summarised in Table 2, with absorptive surfaces referring to hexagonal pyramid absorber surface, and the reflective surfaces the remaining surfaces. The values for the absorptive surface are similar to that of the Solar Two receiver (Pacheco, et al., 2002), while the reflectivity assigned to the reflective surface is a value standard for high quality mirrors (Butel, et al., 2011).

Table 2
Optical properties of the absorptive and reflective surfaces of the receiver.

	Reflectivity	Transmissivity	Slope error	Specularity error
Absorptive	0.05	0	0.95	0.2
Reflective	0.95	0	0.71	0.14

3.5 Absorber thermal setup

For the absorber thermal analysis, a representative section of the total absorber is used, which was assumed to be at the centre of the absorber. A model like the one displayed in Fig. 2 was constructed, but simplified by cutting the geometry such that symmetry boundaries can be applied to resemble the entire hexagonal pyramid, to form the computational domain illustrated in Fig. 7, with Fig. 7a and Fig. 7b displaying geometry with and without the air domain respectively. The air domain allows for radiative heat transfer between the pyramid surfaces, as well as thermal re-radiation losses to be captured. For the ease of meshing, the geometry is divided into different sections, which is clearly visible in the illustration. It should be noted that the central pipe of the absorber element is tubular (a diameter of $D = 10mm$ for the test case), even though the sectional view given in Fig. 7 gives the illusion of a non-tubular central pipe.

For the computational setup, three material property sets were defined: molten salt in the form of solar salt ($NaNO_3$-KNO_3), carbon steel (0.08 C, 0.3 Mn) and air. For the property values, refer to Table 3 and Table 4. Since natural convective heat transfer is a complex heat transfer phenomenon to solve numerically, and not considered for this study at the surface between the pyramid surface and the air due to the assumption that the design makes it negligible, the air was set as a transparent solid, hence the dynamic viscosity not added. The solar salt properties were given to the HTF (and it was also the only fluid of the model), while the carbon steel properties were given to the pyramid shell, and the air property given to the remaining domain outside the pyramid shell, as indicated in Fig. 7.

Table 3
Material properties of the hexagonal pyramid absorber computational model, with the expressions as function of temperature, T [K]

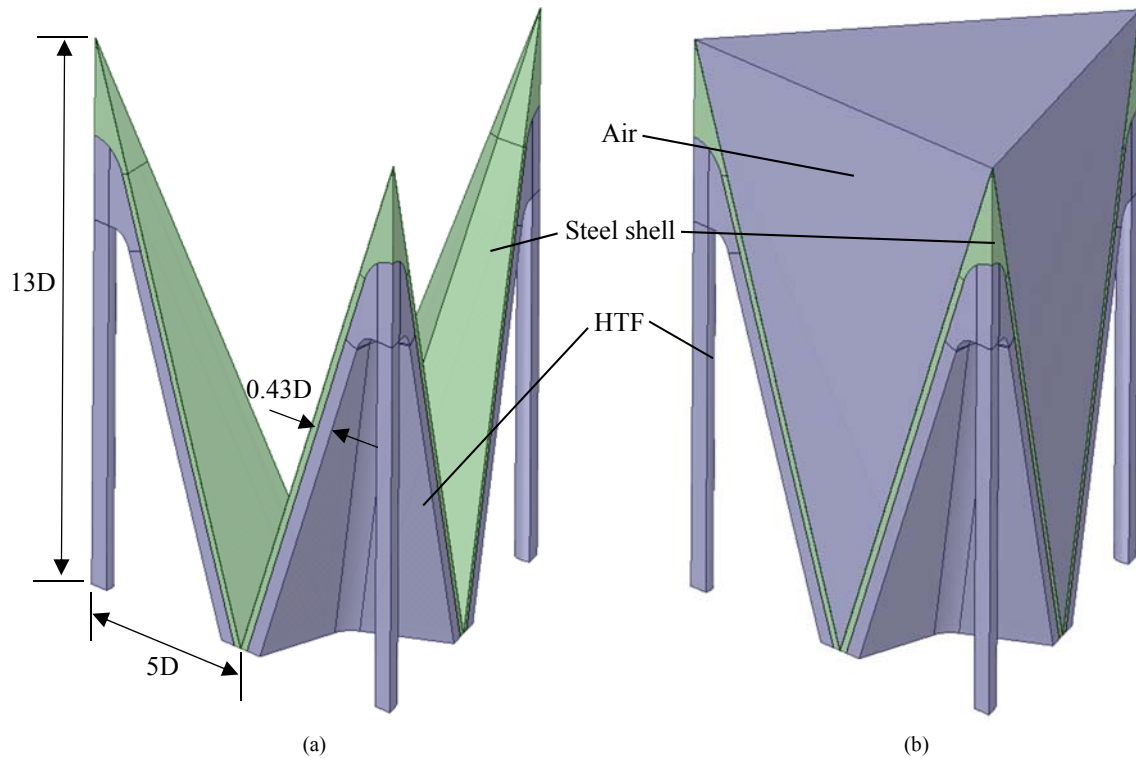|	Density, ρ [kg/m³]	Specific heat, C_p [J/kg·K]	Thermal conductivity, k [W/m·K]	Dynamic viscosity, μ [kg/m·s]	Reference
Solar salt	$2263.641 - 0.636T$	$1396.044 + 0.172T$	0.45	$0.07543937 - 2.77 \times 10^{-4}T + 3.49 \times 10^{-7}T^2 - 1.47 \times 10^{-10}T^3$	(Serrano-López, Fradera, & Cuesta-López, 2013)
Carbon steel	8030	502.48	Piecewise-linear function (refer to Table 4)	-	(Morrell, 2017; ANSYS, 2018)
Air	1.225	1006.43	0.0242	-	(ANSYS, 2018)

Fig. 7. Computational model geometry of the representative hexagonal pyramid absorber with (a) displaying the domain with the solid shell displayed in green, and HTF domain in grey, while (b) shows the same geometry, but with the added air domain simulated as well.

Table 4
Piecewise-linear values for the thermal conductivity of carbon steel (Morrell, 2017)

Temperature [K]	Thermal conductivity, k [W/m·K]
273	59
373	58
573	49
773	40
973	32
1273	28

For demonstration purposes, the boundary conditions and cell zones will be considered with a 2-D illustration presented in Fig. 8. As was mentioned earlier, the hexagonal pyramid absorber geometry is divided on some symmetry planes to provide a computational domain that looks like the image presented in Fig. 7. The boundary condition for these symmetry planes are, as expected, symmetry boundary conditions, and are also illustrated in blue (and indicated as nr. 3) in Fig. 8. The walls' heat conducted through on the inside of the pyramid (shown in grey, nr. 4) is assumed to stay in the system. It is also assumed that this region is well insulated, therefore the walls are assumed as adiabatic. The green boundary (nr. 5) is the inlet, with the assumption of a constant velocity profile with an inlet temperature of 290°C, while the outlet boundary is assumed a zero-pressure outlet (indicated with orange, nr. 6) with an average outlet temperature requirement of 565°C. The velocity at the inlet is therefore iterated to obtain the given outlet temperature. This therefore assumes that the desired HTF temperature range is obtained with a single pass through the absorber. The top boundary that caps of the air zone (discussed later), shown in yellow (nr. 1), is assumed as semi-transparent with a diffuse fraction of 1.
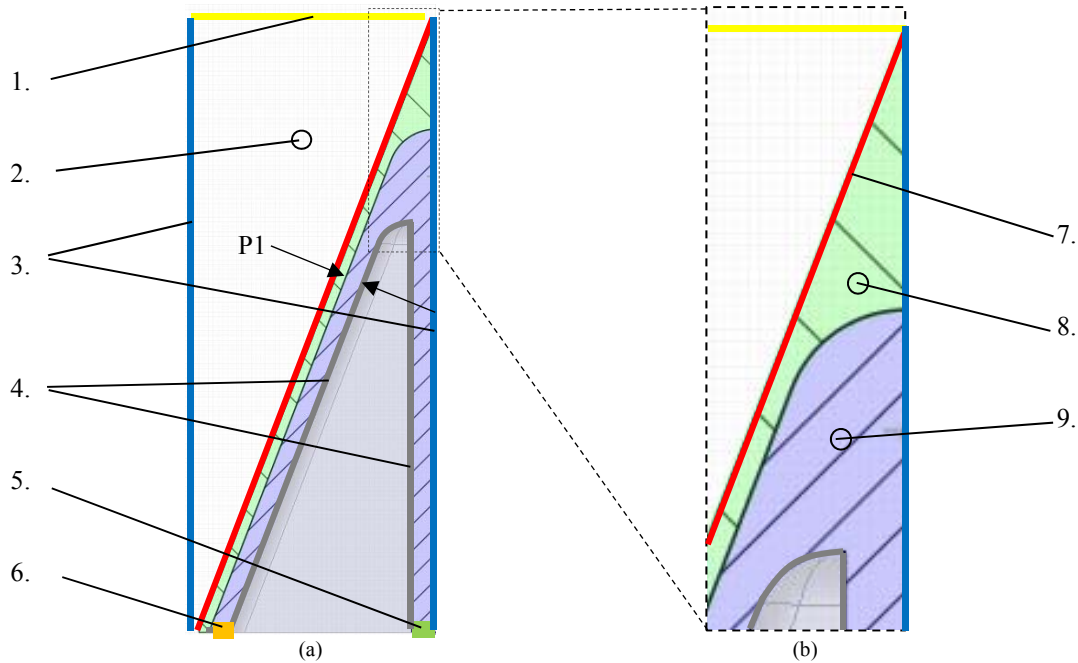
Legend

1.	Transparent boundary	4.	Adiabatic boundary	7.	Heat source zone
2.	Air (solid) zone	5.	Inlet boundary	8.	Steel shell zone
3.	Symmetry boundary	6.	Outlet boundary	9.	HTF (molten salt) zone

Fig. 8. A partial 2-D schematic illustration of the hexagonal pyramid absorber's boundary conditions and cell zones, with (b) displaying a zoomed-in section indicated in (a).

The computational domain consists of four zones: the air outside the absorber (nr. 2), the steel shell structure of the absorber (nr. 8), the molten salt HTF (nr. 9) and the heat source region. Of all these regions, the air is the only zone that participates in radiation to simplify the simulation process. It is this region that is also given the solid air properties listed in Table 3. All the shell boundaries neighbouring the air zone were given an internal emissivity of 0.95, with Kirchhoff's law of thermal radiation assumed stating that the absorption coefficient is equal to the emissivity if the surface emits diffusely. The heat source zone, which is sandwiched in between the air zone and the steel structure, is a region given the same properties as the steel shell structure but is separated to provide the heat source for the simulations. An energy source or power density term is applied to this zone, where the solar heat source is interpolated on. The flux obtained from the optical analysis will be divided by the thickness of the heat source region to obtain a volumetric heat source flux that can be applied to the region. The implementation of an interpolation file as heat source was done previously by Craig, et al. (2010) and Moghimi (2017). The interpolation of the heat source deviated only by 0.95% from the source file when comparing the flux heat generated; assurance that the interpolation was done accurately.

For the CFD model settings, a validation study was conducted to determine an appropriate RANS model that would accurately simulate impinging heat transfer for the viscous model. This resulted in the Transitional SST model, with the Production Kato-Launder and Production Limiter activated. For more information on jet impingement on a concave surface, refer to Lee, Chung, & Won (1999), the study to which the validation was compared. The radiation model selected was the Discrete Ordinates (DO) method. In each quadrant, the polar (θ) and azimuthal (ϕ) angles were divided into three divisions as control angles with three subdivisions (pixels) for each angular discretization, respectively. This implies that 72 ($8 \times 3 \times 3$) extra equations are solved, in addition to the mass, 3 times momentum, energy and 4 times turbulence model equations. The DO equations are only solved in the transparent, solid air, as mentioned before, with no flow or turbulence being solved in this region. All the radiation emitted was also assumed to be diffuse.

4   Results

4.1   Optical analysis

4.1.1   Aperture analysis

The distribution of the solar flux incident on the aperture is important to analyse, since it can give perspective on the extent of the coverage of the absorber area, and how a receiver design can be adjusted to perform better given the heliostat field's distribution. For this study the aperture is defined as the area in front of the opening of the secondary collector of the receiver. The aperture's position, for example, could influence the performance of the receiver, and therefore the entire system. A sensitivity study conducted on the aperture angle revealed that the optimal angle for the PS-10 field was 23.8° measured from the horizontal, almost double the existing design's aperture angle. It should however be added that the analysis only used the solar noon over an entire year using ray-tracing and validating the results using a trigonometric approach, only taking the location of the heliostats relative to the receiver into consideration. A rounded figure of 24° was therefore assigned to the aperture angle and will be used for all other analyses. The extent of the influence of the sun's position is also analysed to get an understanding what distribution is best represented for a year-round performance analysis. When analysing the aperture flux distribution for a given day, as can be viewed in Fig. 9 for five representative times, it is visible that the flux shape changes throughout the day, with the morning hours producing a flux skewed to the left, and as the day progresses the angle turns to the right. As expected, the intensity of the flux also increases up to noon, after which it decreases again.
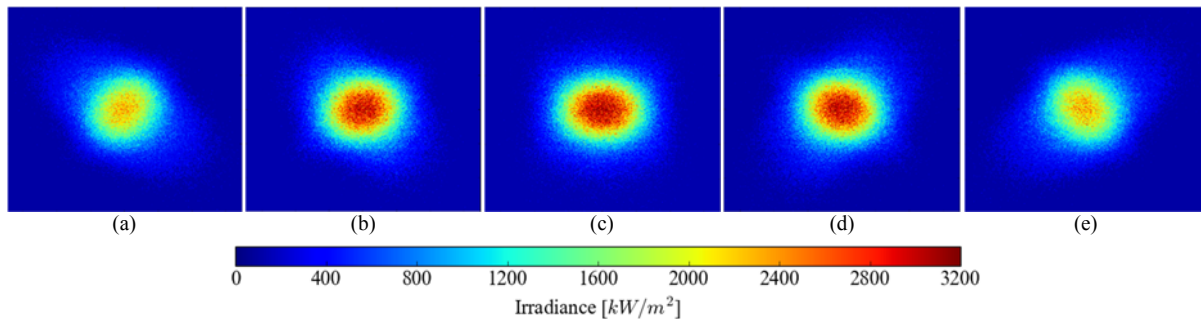

Fig. 9. Solar flux distribution [W/m²] on the aperture of the PS-10 heliostat field constructed in Seville, Spain using SolTrace Monte Carlo ray-tracing for the 180th Julian day at hours (a) 8:00 LAT; (b) 10:00 LAT; (c) 12:00 LAT; (d) 14:00 LAT; and (e) 16:00 LAT.

These flux changes based on time was compared to the average aperture flux distribution over an entire year by analysing every 5th day between 8:00 LAT and 16:00 LAT with 2-hour intervals, with every analysis simulated with 10^6 rays (refer to Fig. 10). When compared, it was concluded that the average flux is most representative to the noon flux on an equinox day. Therefore, the solar noon on the first equinox day was chosen as the representative flux for other analyses. This however only considers the shape of the flux, and not the intensity for a year-round, since the solar noon on an equinox day does not necessarily represent the average flux throughout the year. Fig. 10 also shows the non-concentric nature of the concentrated radiation, although it does have a Gaussian-like distribution, as is evident from the subplots, as well as the percentage flux captured inside the respective circles.
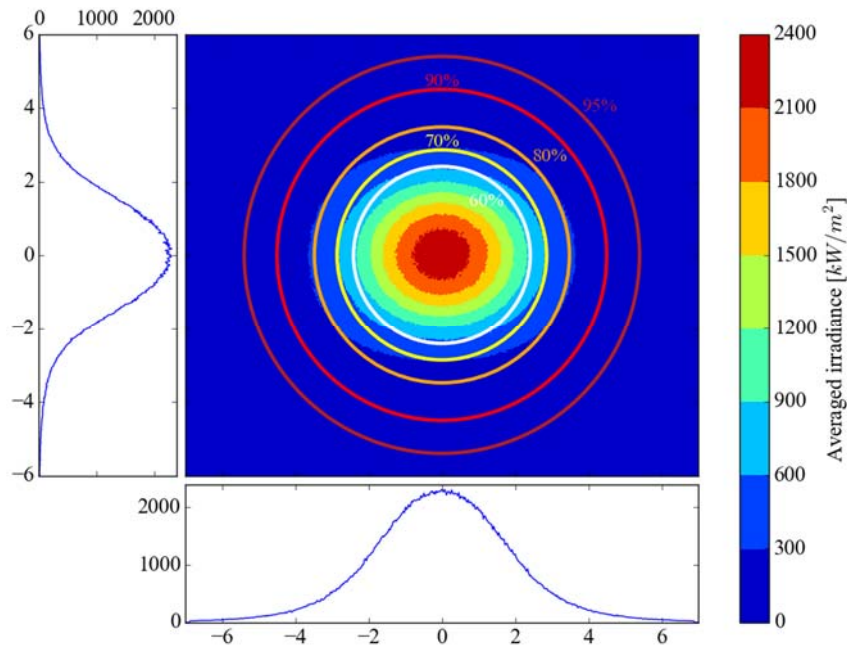
Fig. 10. The average aperture flux distribution [W/m^2] over an entire year at different times of the day, displayed with circles illustrating the percentage flux of the current PS-10 central receiver aperture that is within the circle. Plots on the side and bottom show the flux distribution at the central axes.

4.1.2   Receiver analysis

The original receiver design has an aperture of 1 m and is intended as a multi-unit design. This design can, however, be inflated to larger dimensions to fulfil the role of a single receiver. A comparison study was therefore conducted between the original design (1 m diameter aperture) and a receiver with inflated dimensions, with dimensions inflated to accommodate 90% of the flux concentrated (refer to Fig. 10), therefore a receiver with a 9 m diameter aperture, to analyse whether a change in the flux distribution at the aperture has a significant effect on the flux on the absorber surface. The 1 m diameter aperture opening has a relatively constant flux compared to the 9 m diameter aperture opening with a Gaussian-like distribution. Ray independence was reached at 30×10^6 rays. Referring to Fig. 11, the comparison study revealed that the original case showed a much more evenly distributed flux distribution at the absorber plane, with a relatively constant flux at the aperture opening (Fig. 11a), compared to the inflated design, with the Gaussian-like distribution at the aperture opening (Fig. 11b), although the distribution is still not ideally equally distributed. The magnitude of the flux also differs much, with the original case study almost reaching a 2 MW/m^2 maximum flux, while the other design fails to reach 1.4 MW/m^2. Take note that the absorber surface was replaced with a flat surface approximation to study the approximate flux distribution just above the absorber surface.
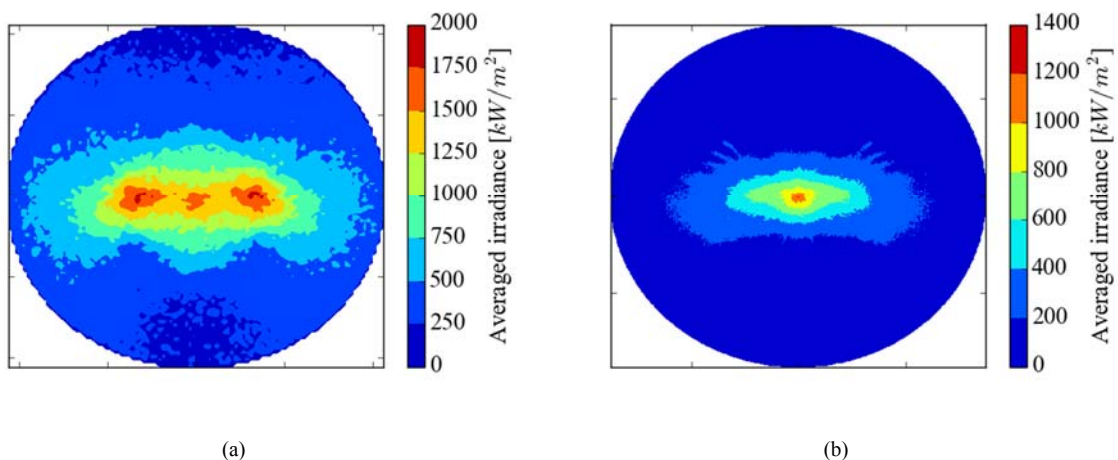

(a)   (b)

Fig. 11. Flux distributions [kW/m^2] above the absorber surface of the (a) original (1m aperture) and (b) inflated (9 m aperture) receiver design, respectively. The absorber surfaces are not plotted to scale, and should represent circular plots.

When comparing the receiver's solar collection efficiency (aperture-to-absorber efficiency), the results show an uncompetitive 68% and 66% efficiency for the original and inflated design respectively; the low percentages caused by high number of reflections the incoming rays experience before reaching the absorber (since the absorptivity of the reflective surfaces is less than 1). A sensitivity study was conducted to reveal the effect of the absorber position on the collection efficiency (refer to Fig. 12) for both tested receiver-designs. Both designs showed dramatic improvements in efficiencies as the distance between the absorber and the aperture narrowed, with efficiency-increases of up to 11-12%, which is directly influenced by the reduction of reflection surfaces between the aperture and the absorber. The shift in the position also has an influence on the flux distribution on the absorber (refer to Fig. 13). It can be noted that the overall flux irradiance lowers, and the peak values shift to the side of the absorber as the position is shifted towards the aperture. This lowered irradiance is a result of the increased absorber surface area available, while the flux peaks shift visualises how the flux is reflected within the receiver. This study also showed that the optics of the receiver is not solvable by changing a single parameter, but rather indicates that adjustments to the design could drastically improve the results of the receiver.

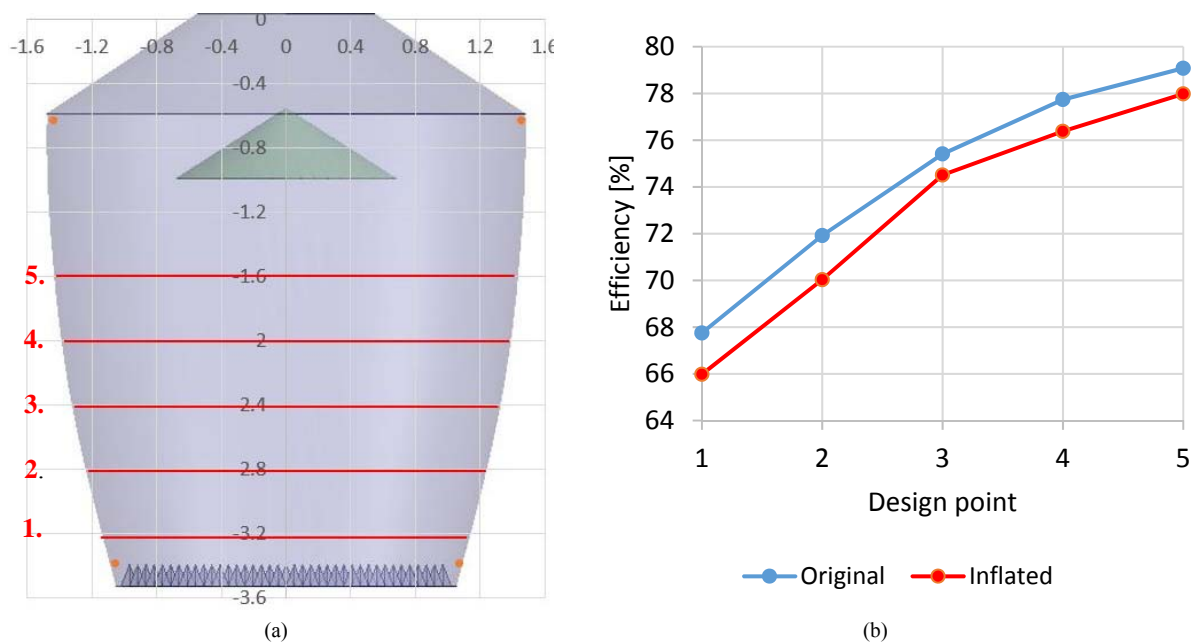(a)   (b)

Fig. 12. (a) The original receiver design with a dimensional grid (units in meters), displaying in red the different positions of the absorber analysed; and (b) a graphical representation of the change in efficiency for the different positions of the absorber.
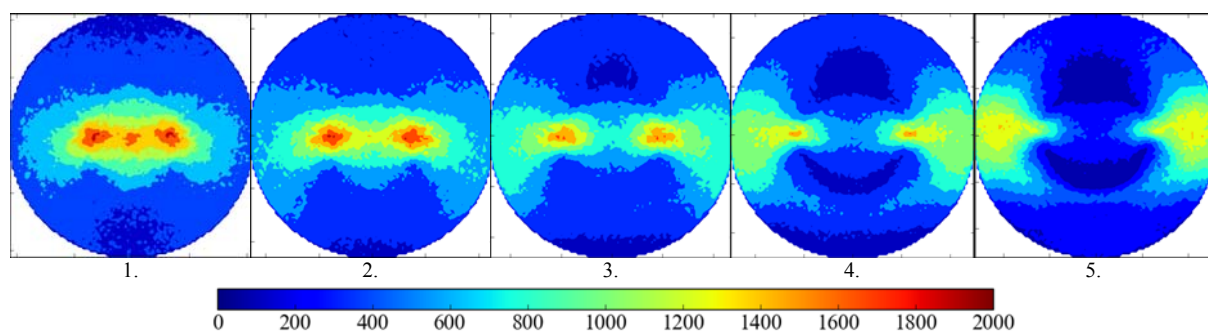

Fig. 13. Flux distribution [kW/m^2] of the absorber for different design points for the original for design points 1 to 5.

4.1.3   Absorber analysis

Although the flat surface approximation provides a good understanding of the flux incident on the absorber, it does not show how the flux interacts with the surface of the absorber with its pyramid-type elements. Therefore, the receiver was simulated with the detailed absorber by applying the discretization method discussed in chapter 3.4. To get a detailed flux on the surface, the surface was simulated by generating 0.64×10^9 rays, which resulted in the flux displayed in Fig. 14. When comparing the flat surface approximation (Fig. 11a) with the detailed absorber surface (Fig. 14b), the general pattern of the flux is visible and comparable, although the lack of detail showed by the flat surface is clearly visible. It is also clearly noticeable that there are massive flux differences on the pyramids themselves, with the tip flux being up to four times greater than that of the valleys. There also seems

to be an asymmetry on the elements as one moves further away from the centre, which is not ideal. The flux irradiance on the flat surface is also much higher than the flux on the absorber, which is a direct consequence of the increased absorber area created by the pyramid design.
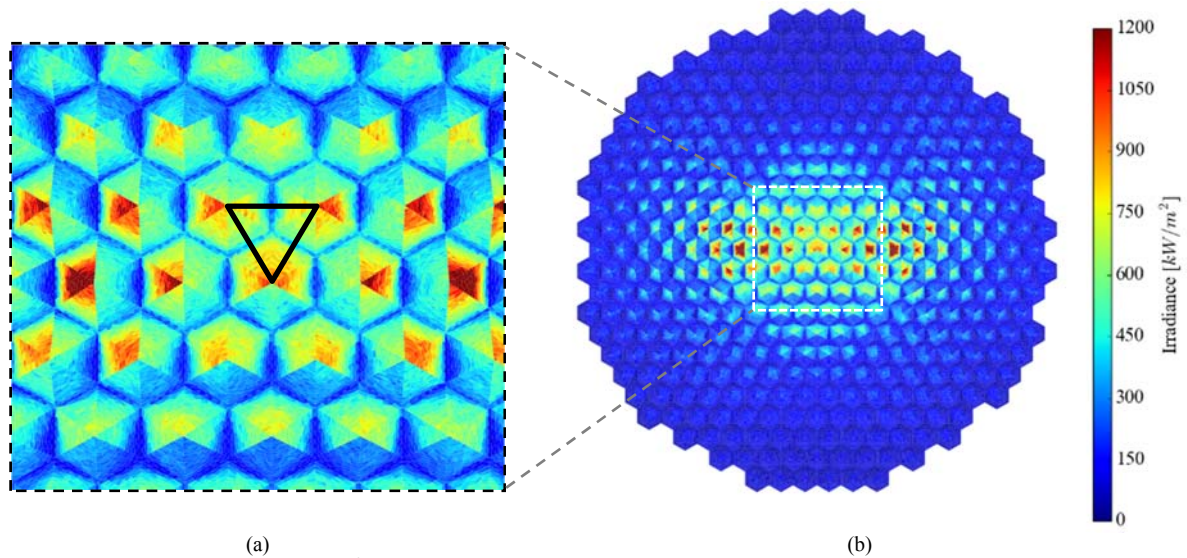

<div align="center">(a)   (b)</div>

Fig. 14. A detailed flux distribution [kW/m²] on the absorber surface of the receiver, with the black triangle indicating the flux area to be used as heat source, (b) displays the entire absorber surface area, with (a) illustrating a zoomed-in image of the flux profile at the centre. Refer to Fig. 6d for an isometric view of the flux distribution.

For the thermal analysis, a representative region needs to be chosen that can be applied as heat source. A region at the centre of the absorber was chosen (black triangle in Fig. 14a), which is representative for an equally distributed solar flux profile due to its symmetry. A detailed flux profile was generated for that region's surface by generating a ray-independent profile by simulating the entire model setup (heliostats, secondary reflector and absorber surface) with 5.91×10^9 rays. A mesh size (using ANSYS mesher as explained in *section 3.4*) was also chosen that could capture the flux distribution adequately without simulating too many elements. This resulted in the detailed distribution shown in Fig. 15.
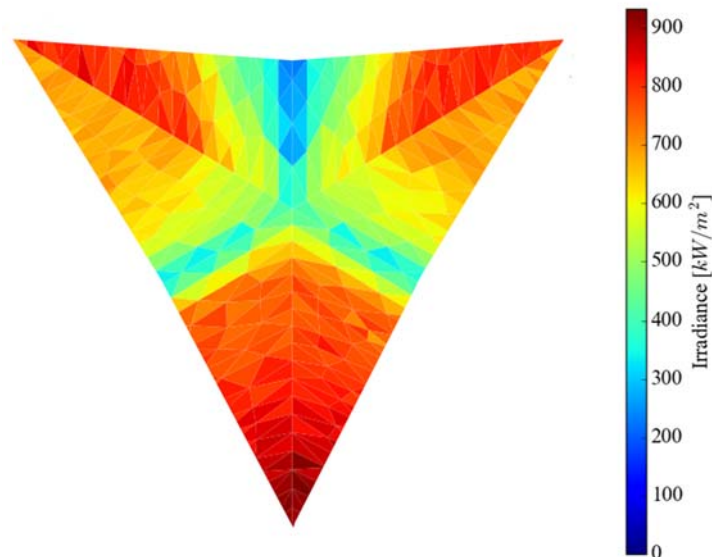

Fig. 15. Detailed flux profile [kW/m²] on the pyramid sides as is indicated by the black triangle in Fig. 14a, generated with Monte Carlo ray-tracing.
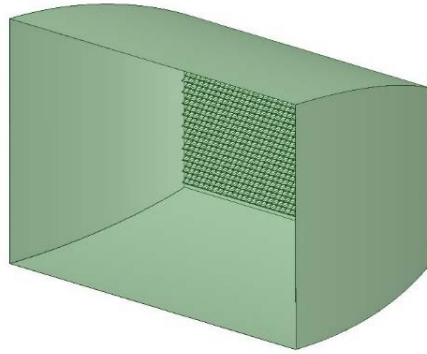
Fig. 16. The optically improved receiver design in a 3-D view.

The optical results have shown aperture-to-absorber efficiencies that are impractical, despite their advantages of thermal loss reduction and prevention. The work of Timinger, et al. (2000) inspired a design with as goal to maximise the aperture flux reaching the absorber, while creating a cavity to prevent thermal losses and keeping the absorber design the same. This resulted in a design displayed in Fig. 16. Timinger, et al. (2000) concluded that secondary concentrators with rectangular apertures and concentrator outlets performed the best. That knowledge was applied in combination with CPC design by considering the maximum shadow line angle, which for the PS-10 field is 45° in the vertical direction, and approximating the horizontal acceptance angle to 120°, that resulted in the design.

Initial optical tests were conducted, and the aperture capture efficiency value caculated to be 79.2%, a value that is dependent on the aperture size (11.9 × 7.5 m aperture dimensions), which can be increased by inflating the receiver dimensions. The aperture-to-absorber efficiency resulted in a value of 93.1%; a dramatic improvement to the original design. Also, the flux distribution on the absorber (refer to Fig. 17), when compared to the original design absorber flux distribution (Fig. 11a), is not only more evenly distributed, but the flux average is also more than double the original design and spread over an area of over 15 times larger than the original design. Although the design does not enclose the absorber as much as the test case design, the CPC as well as absorber design hopes to still reduce the thermal losses substantially. If required, the flux distribution can be more evenly distributed using aiming strategies from the heliostat field.
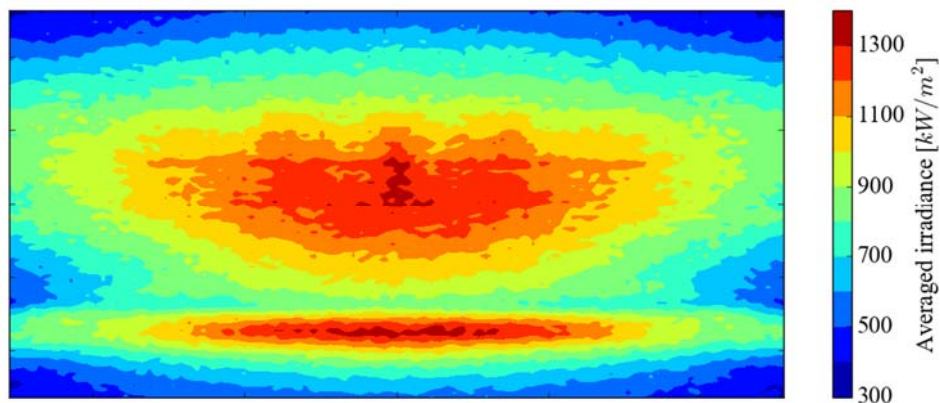

Fig. 17. Flux distribution on the absorber of the new proposed design.

4.2   Thermal analysis
For the thermal analysis, the case study was analysed together with a sensitivity study for the inlet velocity as well as the channel thickness parameter (P1) using the procedure described in *section 3.5*. The parameter P1 is indicated on Fig. 8a.
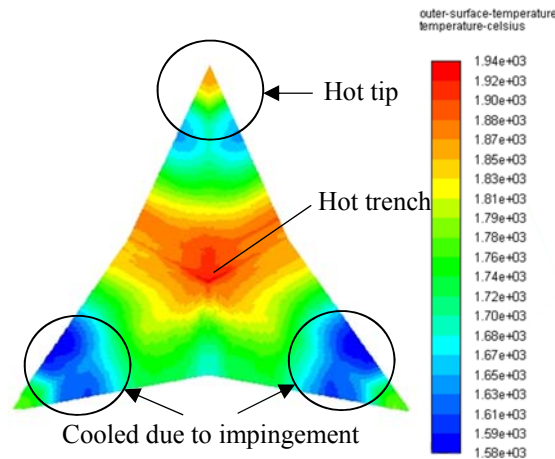
Fig. 18. Temperature distribution [°C] on the surface of the representative pyramid absorber model.

As was discussed in the *Absorber thermal setup*, iterations were done on the inlet flow velocity to achieve the required outlet flow. This approximated to a flow velocity of 0.085 m/s. The focus of this investigation is on the limiting of thermal losses, which are predominantly linked to the surface temperature. When referring to the temperature distribution on the surface of the pyramid (Fig. 18), one will note that temperatures exceed the melting point of carbon steel (1425-1540°C), which makes the current design impractical. This is due to the poor heat transfer capabilities of the current design as well as the low thermal conductivity of the solar salt, evident with the sharp temperature gradient angle visible in Fig. 19 – zoom area 2. Fig. 18 does, however, give an indication of the heat transfer dynamics involved with this design. As the design intended, the impinging cold fluid cooled most of the tip to cooler temperatures compared to the rest of the design. Also, the hottest temperatures are observed at the base, which was also expected and intended, since the design would like to limit the re-radiation by having the hottest regions at the places with the smallest view factor to the ambient. The spike at the tip, however, provides concerns by also showing high temperatures that allow re-radiation losses. This could be due to the excessive material between the impinging fluid and the outer surface, limiting the heat generated at the tip to get to the HTF. This can be seen in Fig. 19 -zoomed area 1, and this could be solved by eliminating the excess material by letting the outer surface run parallel to the inner surface (proposed boundary in figure).
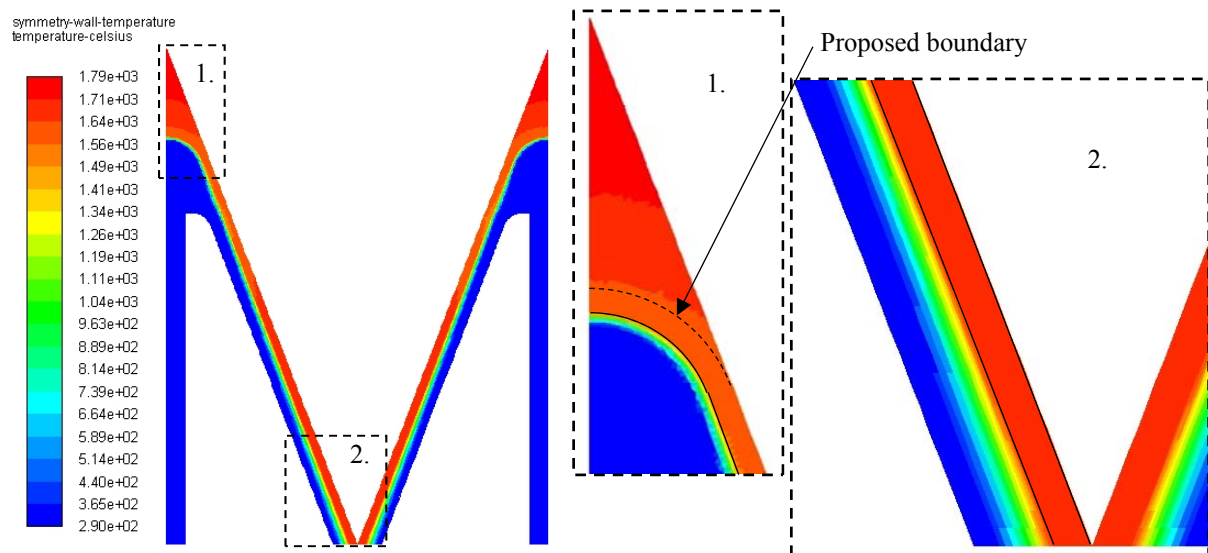

Fig. 19. Temperature distribution [°C] of the thermal computational model at one of the symmetry boundaries.

To get a good appreciation of the losses involved with temperatures on the surface (which is with this model predominantly due to emission losses), a distribution plot was made (refer to Fig. 20) using equation (3):
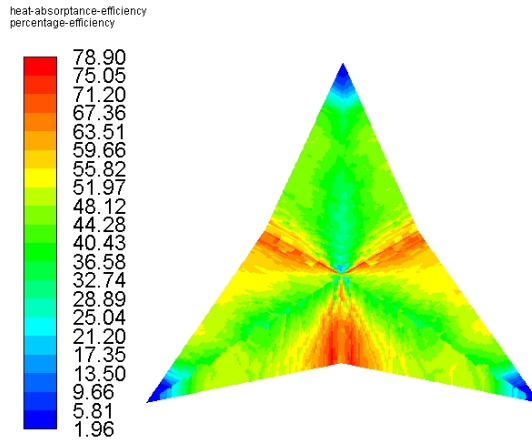
Fig. 20. Contour plot of the efficiency [%] at which the flux incident on the surface of the hexagonal pyramid absorber is extracted or utilized.

$$\mu_{thermal} = \left(1 - \frac{\dot{Q}_{rad}}{\dot{Q}_{tot}}\right) \times 100 \qquad (3)$$

Fig. 20 confirms the concerns at the tips, with only 2% of all energy incident on the tip eventually extracted, although the high temperatures at the trenches do not contribute to that much emission losses, which, as was discussed, has to do with the limited view factor at the trenches. The distribution also roughly illustrates the average efficiency of the absorber design, which is at 48.3%. This is predominantly due to the average outer surface temperature being excessively high (at about 1780°C), which can be assigned to the poor heat transfer of the design.

4.2.2 Inlet flow velocity sensitivity study

The case study has indicated that the current design is not practical. Changes to the design or requirements could improve the design, of which one is the inlet flow velocity. By increasing the HTF flow, the effects of the impinging flow heat transfer as well as the convective heat transfer will increase, which reduces the surface temperature and therefore the re-radiation losses. This, however, comes at the expense of lowering the outlet temperature as well as increasing the pressure drop. The effect of an increase in the flow velocity on the outlet flow temperature, average surface temperature, thermal losses and pressure losses are displayed in Fig. 21. An increase in the inlet flow velocity rapidly reduces the outlet flow temperature, again illustrating the design's poor heat transfer to the fluid. The increase in flow does, however, reduce the average surface temperature, although not as rapidly as the outlet temperature. The correlation between the average surface temperature and the thermal losses is distinct, with the thermal losses in Fig. 21b showing a similar trend to the average surface temperature in Fig. 21a. As was mentioned earlier, the thermal loss reduction comes to the expense of an increase in pressure drop (Fig. 21b), which requires extra pumping power. As typical in heat exchangers, there is therefore a trade-off between the thermal efficiency and the pressure drop. This trade-off can be done by non-dimensionalising the variables (dividing by their maxima, in this case), and obtaining the minimum after adding the values (curve illustrated in Fig. 21b in grey). This shows that for this design an optimal point occurs at approximately 2 m/s.
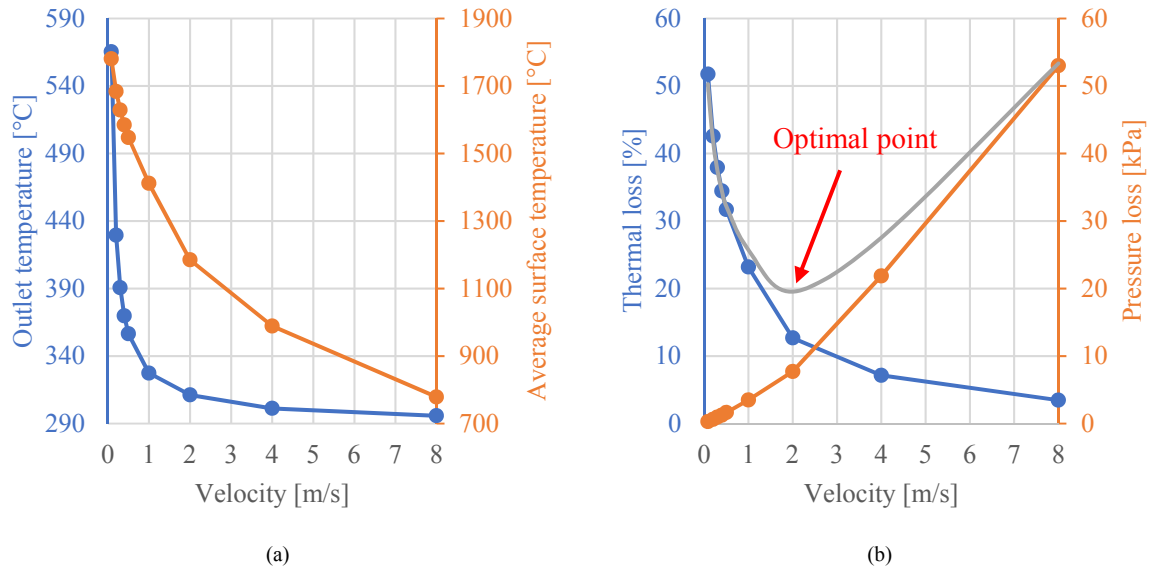
(a)   (b)

Fig. 21. Graphical representation of the effect the inlet velocity [m/s] has on (a) the outlet temperature [°C] and average surface temperature [°C], as well as (b) the thermal [%] and pressure [Pa] losses. Displayed with the grey line is the optimization curve illustrating the non-dimensional adding of the two variables.

By re-evaluating the surface temperature and efficiency of the design at the optimum point at an inlet velocity of 2 m/s (Fig. 22), one can get a better idea of the performance of the absorber with an improved design. When referring to Fig. 22a, the temperature distribution looks similar to the one presented in Fig. 18, although the temperatures are below the melting point of carbon steel, except for the tips, again emphasising the tip's reluctance to successfully transfer heat. This is also reflected in the efficiency of heat extraction displayed Fig. 22b, where the tips give the lowest performance with values being as low as 22.7%. In general, the efficiency at which the heat is extracted is higher than the first analysis (87.3 average). This is mainly due to the low surface temperatures not permitting such a high radiation loss to occur. It is interesting to note when comparing the two efficiency plots with one another, that the efficiency at the regions close to the impinging zone now provide the highest values with the optimal flow analysis, which was not evident for the first analysis. What is even more surprising is that the efficiency exceeds 100%. This may be explained by the fact that the enhanced heat transfer caused by the impinging flow causes heat from the surrounding regions to redirect and cross this boundary through conduction, resulting in heat fluxes higher than the local heat flux generated in that region. With an increase in flow comes an increase in the impingement heat transfer, as shown in Fig. 22b. It also illustrates that the heat transfer in the valleys should be improved, which can be done by adding thermal fins like the design of Garbrecht, et al. (2013), for example.

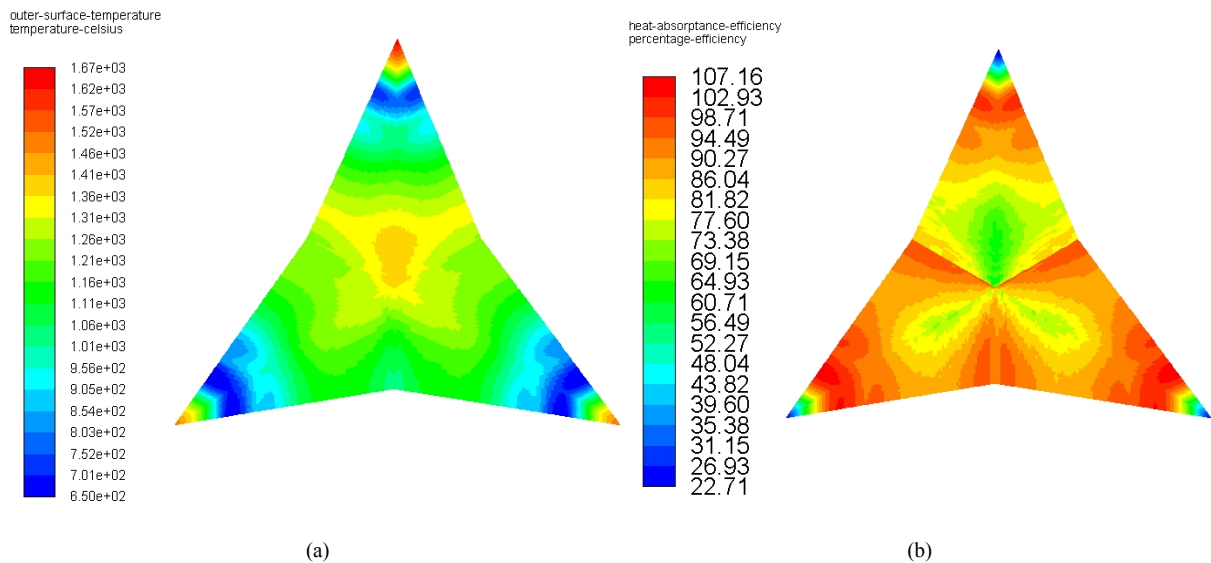(a)   (b)

Fig. 22. Contour plots of the (a) temperature distribution [°C] and (b) efficiency [%] at which the flux incident on the surface of the hexagonal pyramid absorber is extracted or utilized. Inlet velocity = 2 m/s.

4.2.3   Channel thickness (P1) sensitivity study

The limited heat transfer witnessed in the valley regions of the absorber design seen in Fig. 22b, as well as the large temperature gradient seen in Fig. 19 – zoomed area 2, inspired a study of the effect the channel thickness parameter P1 could have on the performance of the absorber. By narrowing the exit channel's thickness through which the HTF flows, more fluid gets exposed to the heated surface, therefore limiting the effect of the poor heat transfer properties of the molten salt. An excerpt of that study is presented here, with the parameter P1 chosen as a quarter of the original design. By employing the same boundary conditions and requirements, the inlet flow velocity increased by a factor of 1.82 to 0.155 m/s to maintain the required outlet temperature. A summary of these results is displayed in Table 5.

Table 5
Summary of the results of the original test case compared to the current case where the P1 channel thickness parameter was reduced.

Case	Inlet velocity [m/s]	Outlet temp. [°C]	Outer surface temp. avg. [°C]	Pressure loss [kPa]	Thermal efficiency, $\mu_{thermal}$ [%]
Test case	0.085	565.4	1780	0.28	48.26
New ($\frac{1}{4}P_1$)	0.155	563.9	1107	13.0	88.54

The results displayed in Table 5 generally shows an immense improvement in results, with the most noticeable of the results being the thermal efficiency improving by almost double to 88.5%. This is due to more fluid flowing close to the heated surface, which causes the fluid to heat up much quicker, as well as decreasing the surface temperature that as knock-on effect reduces the re-radiation losses. The increased flow also adds to the additional enhanced heat transfer. This, however, comes with the price of a corresponding large increase in pressure drop required to push the flow through the thin channel. In the previous parameter sensitivity study, the 2 m/s fluid flow case showed a similar thermal efficiency of 87%, but had a 40% less pressure drop. The reduction in channel thickness therefore has the great disadvantage of causing a large pressure drop, but with the advantage of creating a thermally efficient absorber with a temperature outlet that meets the requirements. These results only emphasises the small adjustments that can be made to improve the current absorber design and the inevitable compromises that must be found when designing these types of absorbers.

5   Technical evaluation

For an overview of the results obtained, the performances of the different stages of the receiver as well as the entire system simulated are summarised in Table 6. The table is a summary of the original design, which shows the results of the benchmark test cases, the improved design, which showcases the best results after sensitivity studies, as well as the performance results of the new proposed optically improved rectangular design. It should be noted that the results displayed in the *Improved design* section only considers the results that were obtained for the cases that met the minimum requirements. The *New proposed design* also assumes that the optical and thermal performance results are independent, and that the thermal performance conducted applies to the new design. The receiver efficiency was calculated by considering only the aperture-to-absorber efficiency (which is the effect the secondary collector has on the receiver) and the thermal efficiency.

The table portrays a strong image of the low efficiencies (32.8% receiver efficiency) at which the original design would function. It also shows that the few sensitivity studies that were conducted already showed significant improvement, more than doubling the original receiver's efficiency. From the analysis, there are limited improvements that can still be made on the field-to-aperture efficiencies when looking on the receiver side, with the majority of the improvements to be made by improving the field efficiency. The aperture capture efficiency relies predominantly on the aperture area, and for design's purposes this is also mostly limited, and can be easily increased by inflating the dimensions of a design. This would, however, put strain on the structure design. The efficiencies therefore mostly rely on the design of the secondary reflector or cavity, as well as the performance of the absorber, especially with the proposed design. The authors' new proposed receiver design, which mainly changes the design of the secondary reflector, greatly improves the overall performance of the receiver design, with an estimation of over 12% improvement to over 82% receiver efficiency. The sensitivity analysis done for the absorber thermal analysis has shown that much improvement can still be made for the thermal performance of the current absorber design, which would also greatly improve the design's efficiency, which results in a competitive prospect as receiver. As was mentioned in earlier chapters, values obtained for receivers at plants such as Solar Two (85.6-88%) (Pacheco, et al., 2002) and the MSEE (cavity measurements ranging from 86-88%) (Bergan, 1986) is greater than the receiver efficiencies calculated for all designs tested in this study. Preliminary

sensitivity studies on selected parameters have shown that great improvements can still be made to the receiver design to make it a prospective competitive receiver design.

Table 6
Summary of the performance values (in percentages) for the different stages of the central receiver system.

	Field-to-aperture efficiency [1]	Aperture capture efficiency [2]	Aperture-to-absorber efficiency [3]	Thermal efficiency [4]	System efficiency (before power cycle) ([1] × [2] × [3] × [4])	Receiver efficiency ([3] × [4])
Original design [a]	85.2*	90**	68	48.3	25.19	32.84
Improved design [b]	86	90	79	88.5***	54.11	69.92
Change in performance ([b]-[a])	0.8	-	11	40.2	28.93	37.07
New proposed design [c]	86	79.2	93.1	88.5****	56.12	82.39

*	Value deducted from optimal performance obtained and change in performance from original aperture angle.
**	Assume efficiency of inflated receiver design, since small design could be part of a fly-eye or similar design.
***	Only considered performance values of cases that fulfilled all requirements.
****	Assumed the thermal efficiency obtained in [b].

6   Conclusion and outlook

The approach of numerically modelling the solar position, DNI, and sun shape with an existing heliostat field (PS-10 field) to analyse a receiver for a solar tower CSP system was considered rather than assuming a flux to provide a more accurate approach for receiver performance analyses. The implemented Iqbal solar tracking model compared well with other more accurate models, while the clear sky parameterisation C model by Iqbal (1983) provided a realistic DNI fluctuation to approximate the irradiance. This combined with the PS-10 field provided a realistic aperture flux, assuming a single point aiming strategy. The study concluded that the solar noon equinox flux provided a similar aperture flux distribution as the year-round averaged flux distribution. Applying the flux on the receiver design proved that the proposed design's optics provided an impractical aperture-to-absorber efficiency of 68%, although preliminary sensitivity studies showed that slight alterations could drastically improve the optical performance of the design. The absorber's thermal analysis showed similar unconvincing results, with temperatures exceeding structure melting temperatures with efficiencies of 48.3%. Preliminary sensitivity studies, however, showed great promise for improvement with efficiencies increasing up to 88.5% for designs which meet the design requirements. The problems perceived with the optical design inspired a new receiver design, which showed great promise, with the optical efficiencies reaching efficiencies over 93%.
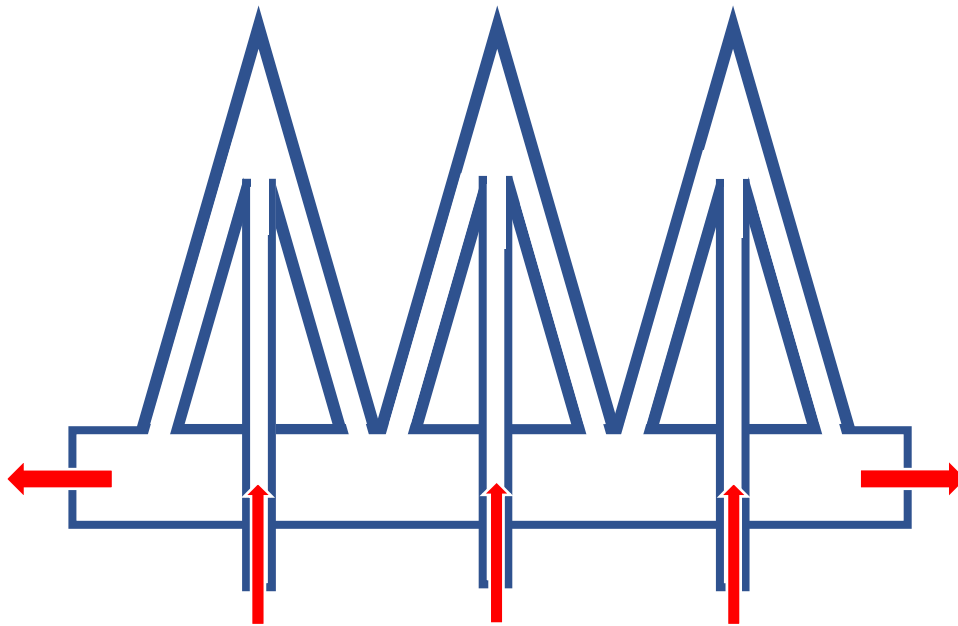
Fig. 23 Schematic illustration of the proposed flow for the receiver design.

This study has shown great promise for the new receiver design with the number of improvements that this design may hold. Further research should be conducted on optimising the optical and absorber side of the design with the sight on improving the efficiency, output, as well as lowering the costs, as well as studying the thermal stresses, production processes as well as a cost analysis. Further consideration should also be given to the plumbing aspect of this design, and how the receiver will be connected to the rest of the HTF cycle. A schematic illustration for a proposed flow of the HTF in and out of the receiver design is shown in Fig. 23. This study focused on improving the accuracy of numerical receiver analyses. This could be improved by implementing more accurate solar position, sun shape and weather prediction models. The thermal analysis can be improved by developing an approach to accurately predict the convective losses.

7   Acknowledgements

8   References

Amsbeck, L., Buck, R., Heller, P., Jedamski, J., & Uhlig, R. (2008, March). Development of a tube receiver for a solar-hybrid microturbine system. *Proceedings of the 14th SolarPACES Conference*, 4-7.

ANSYS. (2018). Academic Research Fluent, Release 19.1.

Avila-Marin, A. (2011). Volumetric receivers in Solar Thermal Power Plants with Central Receiver System technology: A review. *Solar Energy, 85*(5), 891-910.

Bergan, N. (1986). *Testing of the Molten Salt Electric Experiment solar central receiver in an external configuration. No. SAND86-8010.* Livermore, CA (USA): Sandia National Labs.

Bird, R., & Hulstrom, R. (1981). Review, Evaluation, and Improvement of Direct Irradiance Models. *Journal of Solar Energy Engineering, 103*(3), 182-192.

Buck, R., Brauning, T., Denk, T., Pfander, M., Schwarzbozl, P., & Tellez, F. (2002). Solar-hybrid gas turbine-based power tower systems (REFOS). *ASME Journal of Solar Energy Engineering, 124*(1), 2-9.

Butel, G., Coughenour, B., Macleod, H., Kennedy, C., Olbert, B., & Angel, J. (2011). second-surface silvered glass solar mirrors of very high reflectance. *In High and Low Concentrator Systems for Solar Electric Applications VI. 8108*, p. 81080L. International Society for Optics and Photonics.

Chang, Z., Li, X., Xu, C., Chang, C., & Wang, Z. (2014). Numerical simulation on the thermal performance of a solar molten salt cavity receiver. *Renewable Energy, 69*, 324-335.

Clausing, A. (1981). An Analysis of Convective Losses from Cavity Solar Central Receivers. *Solar Energy, 27*(4), 295-300.

Craig, K. J., Marsberg, J., & Meyer, J. P. (2016). Combining ray tracing and CFD in the thermal analysis of a parabolic dish tubular cavity receiver. *In: AIP Conference Proceedings. Proceedings of the 21st SolarPACES Conference 2015, 13-16 October 2015, Cape Town, South Africa, 1734*, 030009.

Craig, K., Harkness, A., Kritzinger, H., & Hoffmann, J. (2010). Analysis of AP1000 Reactor Vessel Cavity and Support Cooling. *European Nuclear Conference.* Barcelona, Spain.

De Wit, C., Goudriaan, J., & van Laar, H. (1978). Simulation of Simulation, Respiration and Transpiration of Crops. 148. Pudoc. Wageningen, The Netherlands.

EASAC. (2011). *Concentrating solar power: its potential contribution to a sustainable energy future.* Germany: German Academy of Sciences Leopoldina.

Eddhibi, F., Ben Amara, M., Balghouthi, M., & Guizani, A. (2015). Optical study of solar power plants. *Journal of Physics: Conference Series, 012018,* 1-7.

European Union. (2007). *Concentrating Solar Power - From Research to Implementation.* Retrieved March 14, 2018, from http://www.solarpaces.org/wp-content/uploads/2007_concertrating_solar_power_en.pdf

Fang, J., Wei, J., Dong, X., & Wang, Y. (2011). Thermal performance simulation of a solar cavity receiver under windy conditions. *Solar Energy, 85*(1), 126-138.

Forsberg, C. W., Peterson, P. F., & Zhao, H. (2007). High-Temperature Liquid-Fluoride-Salt Closed-Brayton-Cycle Solar Power Towers. *Journal of Solar Energy Engineering, 129*(2), 141-146.

Frohlich, C., & Brusa, R. (1981). Solar radiation and its variation in time. *Solar Physics, 74*(1), 209-215.

Frohlich, C., & Wehrli, C. (1981). Spectral distribution of solar irradiance from 25000 nm to 250 nm. Davos, Switzerland: Private Communication.

Garbrecht, O., Al-Sibai, F., Kneer, R., & Wieghardt, K. (2013). CFD-simulation of a new receiver design for a molten salt solar power tower. *Solar Energy, 90,* 94-106.

Hischier, I., Hess, D., Lipinski, W., Modest, M., & Steinfeld, A. (2009). Heat Transfer Analysis of a Novel Pressurised Air Receiver for Concentrated Solar Power via Combined Cycles. *Journal of Thermal Science and Engineering Applications, 1*(4), 041002.

Ho, C., & Iverson, B. (2014). Review of high-temperature central receiver designs for concentrating solar power. *Renewable and Sustainable Energy Reviews, 29,* 835-846.

Iqbal, M. (1983). *An introduction to solar radiation.* Ontario: Academic Press, Inc.

Joly, M., Antonetti, Y., Python, M., Gonzalez, M., Gascou, T., Scartezzini, J. L., & Schuler, A. (2013). Novel black selective coating for tubular solar absorbers based on a sol–gel method. *Solar Energy, 94,* 233-239.

Kesselring, P., & Selvage, C. S. (1986). *The IEA/SSPS Solar Thermal Power Plants — Facts and Figures — Final Report* (1 ed.). Berlin, Germany: Springer.

Korzynietz, R., Quero, M., & Uhlig, R. (2012). SOLUGAS—Future Solar Hybrid Technology. *In Proceedings of the 18th International SolarPACES Conference, Marrakech, Morocco, 11-14 September*, (pp. 11-14).

Kretzschmar, H., & Gauché, P. (2012). Hybrid pressurized air receiver for the sunspot cycle. *In 1st South African Solar Energy Conference (SASEC), Stellenbosch, South Africa, 21-23 May*, (pp. 21-23).

Lata, J., Rodriquez, M., & de Lara, M. (2008). High flux central receivers of molten salts for the new generation of commercial stand-alone solar power plants. *Journal of Solar Energy Engineering, 130*(2), 021002.

Li, X., Kong, W., Wang, Z., Chang, C., & Bai, F. (2010). Thermal model and thermodynamic performance of molten salt cavity receiver. *Renewable Energy, 35*(5), 981-988.

Liao, Z., & Faghri, A. (2016). Thermal analysis of a heat pipe solar central receiver for concentrated solar power tower. *Applied Thermal Engineering, 102,* 952-960.

Lovegrove, K., & Stein, W. (2012). *Concentrator Solar Power Technology, Principle development and applications* (1st ed.). Cambridge: Woodhead Publishing.

Lubkoll, M., Backström, T. v., Harms, T., & Kröger, D. (2015). Initial analysis on the novel Spiky Central Receiver Air Pre-heater (SCRAP) pressurized air receiver. *Energy Procedia, 69,* 461-470.

Moghimi, M. (2017). Dissertation : Optical, thermal and economic optimsation of a linear fresnel collector. *1.* Pretoria, South Africa: Unversity of Pretoria.

Montes, M., Rovira, A., Martínez-Val, J., & Ramos, A. (2012). Proposal of a fluid flow layout to improve the heat transfer in the active absorber surface of solar central cavity receivers. *Applied Thermal Engineering, 35,* 220-232.

Morrell, R. (2017). *National Physical Laboratory: Kaye&Laby.* Retrieved October 15, 2018, from http://www.kayelaby.npl.co.uk/general_physics/2_3/2_3_7.html

Noone, C. J., Torrilhon, M., & Mitsos, A. (2012). Heliostat field optimization: A new computationally efficient model and biomimetic layout. *Solar Energy, 86*(1), 792-803.

NREL. (2018). *MIDC SPA Calculator.* Retrieved 04 20, 2018, from https://midcdmz.nrel.gov/solpos/spa.html

Osuna, R., Olavarria, R., Morillo, R., Sanchez, M., Cantero, F., Fernandez-Quero, V., . . . Talegon, J. (2006). PS10, construction of a 11MW solar thermal tower plant in Seville, Spain. *In: Conference Proceedings of 13th SolarPACES Conference, Seville, Spain, June*, (pp. 20-23).

Pacheco, J., Bradshaw, R., Dawson, D., De La Rosa, W., Gilbert, R., Goods, S., . . . Prairie, M. (2002). *Final Test and Evaluation Results from the Solar Two Project, Report No. SAND2002-0120.* Albuquerque, NM, U.S.A.: Sandia National Laboratories.

Pacio, J., & Wetzel, T. (2013). Assessment of liquid metal technology status and research paths for their use as efficient heat transfer fluids in solar central receiver systems. *Solar Energy, 93*, 11-22.

Pye, J., Zheng, M., Asselineau, C., & Coventry, J. (2014). An exergy analysis of tubular solar-thermal receivers with different working fluids. *In Proceedings of 20th SolarPACES International Conference* (pp. 16-19). Beijing, China: Energy Procedia.

Reda, I., & Andreas, A. (2004). Solar position algorithm for solar radiation appications. *Solar Energy, 76*(5), 577-589.

Reicosky, D., Winkelman, L., Baker, J., & Baker, D. (1989). Accuracy of hourly air temperatures calculated from daily minima and maxima. *Agricultural and Forest Meteorology, 46*(3), 193-209.

Rodríguez-Sanchez, M. R., Marugan-Cruz, C., Acosta-Iborra, A., & Santana, D. (2014). Comparison of simplified heat transfer models and CFD simulations for molten salt external receiver. *Applied Thermal Engineering, 73*(1), 993-1005.

Rodríguez-Sánchez, M., Sánchez-González, A., Acosta-Iborra, A., & Santana, D. (2017). Variable Velocity in Solar External Receivers. *In AIP Conference Proceedings. 1850*, p. 030043. AIP Publishing.

Rodríguez-Sánchez, M., Sánchez-González, A., Marugán-Cruz, C., & Santana, D. (2014). New designs of molten-salt tubular-receiver for solar power tower. *Energy Procedia. 49*, pp. 504-513. Proceedings of 19th SolarPACES International Conference, Las Vegas, Nevada, USA, 17-20 September 2013.

Rodríguez-Sánchez, M., Soria-Verdugo, A., Almendros-Ibáñez, J. A., Acosta-Iborra, A., & Santana, D. (2014). Thermal design guidelines of solar power towers. *Applied Thermal Engineering, 63*(1), 428-438.

Romero, M., Marcos, M. J., Osuna, R., & Fernandez, V. (2000). Design and implementation plan of a 10 MW solar tower power plant based on volumetric-air technology in Seville (Spain). *Proceedings of the Solar 2000 Solar Power Life - Share the Energy*.

Serrano-López, R., Fradera, J., & Cuesta-López, S. (2013). Molten salts database for energy applications. *Chemical Engineering and Processing: Process Intensification, 73*, 87-102.

Singer, C., Buck, R., Pitz-Paal, R., & Müller-Steinhagen, H. (2010). Assessment of Solar Power Tower Driven Ultrasupercritical Steam Cycles Applying Tubular Central Receivers With Varied Heat Transfer Media. *Journal of Solar Energy Engineering, 132*(2), 041010.

Spencer, J. (1971). Fourier series representation of the position of the Sun. *Search, 2*(5), 172.

Timinger, A., Spirkl, W., Kribus, A., & Ries, H. (2000). Optimized secondary concentrators for a partitioned central receiver system. *Solar Energy, 69*(2), 153-162.

Wendelin, T., Dobos, A., & Lewandowski, A. (2013). SolTrace: a ray-tracing code for complex solar optical system. *NREL - technical report, 303*, 275-300.

Yu, Q., Wang, Z., & Xu, E. (2012). Simulation and analysis of the central cavity receiver's performance of solar thermal power tower plant. *Solar Energy, 86*(1), 164-174.